IOP Publishing *Flex. Print. Electron.* **7** (2022) 014011 https://doi.org/10.1088/2058-8585/ac518a

Flexible and Printed Electronics

RECEIVED
5 September 2021

REVISED
1 February 2022

ACCEPTED FOR PUBLICATION
3 February 2022

PUBLISHED
1 March 2022

PAPER

Machine learning-enabled feature classification of evaporation-driven multi-scale 3D printing

Samannoy Ghosh[1,4], **Marshall V Johnson**[2,4], **Rajan Neupane**[1], **James Hardin**[3], **John Daniel Berrigan**[3], **Surya R Kalidindi**[2,*] **and Yong Lin Kong**[1,*]

[1] Department of Mechanical Engineering, University of Utah, Salt Lake City, UT 84112, United States of America
[2] Woodruff School of Mechanical Engineering, Georgia Institute of Technology, Atlanta, GA 30313, United States of America
[3] Materials and Manufacturing Directorate, Air Force Research Laboratory, Wright-Patterson Air Force Base, OH, United States of America
[4] Co-first authors.
[*] Authors to whom any correspondence should be addressed.

E-mail: surya.kalidindi@me.gatech.edu **and** yong.kong@utah.edu

Keywords: 3D printed electronics, feature classification with machine learning, additive manufacturing

Abstract

The freeform generation of active electronics can impart advanced optical, computational, or sensing capabilities to an otherwise passive construct by overcoming the geometrical and mechanical dichotomies between conventional electronics manufacturing technologies and a broad range of three-dimensional (3D) systems. Previous work has demonstrated the capability to entirely 3D print active electronics such as photodetectors and light-emitting diodes by leveraging an evaporation-driven multi-scale 3D printing approach. However, the evaporative patterning process is highly sensitive to print parameters such as concentration and ink composition. The assembly process is governed by the multiphase interactions between solutes, solvents, and the microenvironment. The process is susceptible to environmental perturbations and instability, which can cause unexpected deviation from targeted print patterns. The ability to print consistently is particularly important for the printing of active electronics, which require the integration of multiple functional layers. Here we demonstrate a synergistic integration of a microfluidics-driven multi-scale 3D printer with a machine learning algorithm that can precisely tune colloidal ink composition and classify complex internal features. Specifically, the microfluidic-driven 3D printer can rapidly modulate ink composition, such as concentration and solvent-to-cosolvent ratio, to explore multi-dimensional parameter space. The integration of the printer with an image-processing algorithm and a support vector machine-guided classification model enables automated, *in situ* pattern classification. We envision that such integration will provide valuable insights in understanding the complex evaporative-driven assembly process and ultimately enable an autonomous optimisation of printing parameters that can robustly adapt to unexpected perturbations.

1. Introduction

The synergetic integration of three-dimensional (3D) printing and nanomaterials, also known as multi-scale 3D printing, can create freeform bioelectronic, electrical, and biomedical devices [1] that are otherwise challenging to fabricate with conventional fabrication approaches [2]. Previous work in multi-scale 3D printing has demonstrated the ability to create electronics such as photodetectors, antennas [3], light-emitting diodes [4], and solar cells [5]. For example, an evaporation-driven colloidal assembly can be leveraged in the 3D printing process to control nanomaterial deposition without additional tools, in contrast to printing techniques such as transfer printing. For instance, prior work has demonstrated the ability to entirely 3D print active electronics that involve five layers of distinct materials by leveraging evaporative assembly of the inks [4, 6].

The ability to control printed morphologies is critical to achieving targeted performance and resolution of the printed device [7]. However, consistently achieving the printing of targeted patterns with an evaporative assembly process remains challenging due to the inherent sensitivity of the drying droplets to perturbations. Indeed, evaporative-patterning is driven by a complex self-assembly process governed by flow morphologies and multiphase dynamics. It can generate a broad palette of patterns, such as the so-called ‘coffee ring’ features [8], even with small perturbation in print parameters. Relevant print parameters include ink concentration, composition, polydispersity, surface free energy [9], as well as microenvironmental conditions such as pressure, temperature and humidity [10].

A 3D printing system that can autonomously adapt to perturbation is desirable to consistently achieve a targeted print feature. This is particularly important for the 3D printing of active electronics that involve multiple layers of deposition, as the deviation of the underlying layer will likely generate further deviation of the print layer. The print conditions of the evaporative-driven colloidal droplets govern the flow morphologies of the droplets [11–13] and guide the formation of the nanoparticle patterns. Hence, a parameter control strategy to analyse printed droplets and automatically adjust print parameters could prove effective to achieve targeted patterns. In the past few years, such pro-active process monitoring of 3D printed parts has been demonstrated in additive manufacturing (AM) [14–17]. For example, 3D printing systems augmented with statistical methods [18], process control [19–22], and machine learning (ML) [23–32] have shown promising progress in defect detection, process optimisation of fused filament fabrication (FFF) [33–35] and metal sintering processes [36–38]. Specifically, integration of vision guidance with ML has further enhanced the capability of the systems to perform anomaly detection, classification and optimisation of 3D printing [38–45]. For example, ML guided *in situ* process control has been demonstrated in electrohydrodynamic jet-printing to autonomously tune the applied voltage by monitoring droplet behaviour during jetting [46]. Jin *et al* [27] have shown ML guided computer vision tools to identify line thickness and autonomously adjust the flow rate. Johnson *et al* [43] have described image analysis tools for detecting deviations in spanning filament traces.

As mentioned earlier, printing electronics require evaporative assembly of targeted print patterns through microextrusion. Despite their use in AM systems such as FFF and metal sintering, most of the existing ML tools involve customised solutions. They cannot be readily implemented for parameter control of colloidal nanoparticles due to the complexity of the evaporative patterning process. Existing techniques are often limited to recognising easily distinguishable features such as drop size and line thickness. In contrast to such features, the evaporative colloidal patterns printed through microextrusion exhibit much higher complexity, especially in its drop texture and demonstrate a relatively sensitive dependence with the print parameters. This poses a critical challenge in implementing existing feature recognition systems that can analyse the complex texture patterns and identify the uniqueness and diversity of these patterns.

To address this challenge, microfluidic mixing and custom vision-guided image classification can be combined to map the vast feature processing and ink formulation space. This approach can enable us to optimise the print parameters and gain insights over the complex conditions for targeted multiscale printing. Research to implement such ML guided classification of samples, printed through automated microextrusion of multiple ink compositions, has been unexplored to the best of our knowledge.

Here, we demonstrate a rapidly tunable microfluidic mixer based print platform integrated with ML to classify a broad range of nanoparticle patterns printed by seamlessly switching between ink compositions *in situ*. The integrated printing and imaging platform is schematically shown in figure 1. The print platform, capable of demonstrating a broad gradient of changes, has been achieved through a microfluidic mixer. Microfluidic mixers allow the mixing of different inks at a microscale [47–50]. Existing research has demonstrated the use of microfluidics to switch between multiple visco-elastic inks for high-throughput microextrusion printing [51]. However, to date, a system that can seamlessly control the composition of colloidal nanoparticle inks in an automated way has not been explored. We achieve this by fabricating a herringbone-patterned chaotic microfluidic mixer, as shown in figure 2(a). As a proof of concept, we leverage the fluorescence property of colloidal QDs, which provide a means to rapidly acquire an overall deposition profile. The print platform can be used with a broad range of colloidal nanoparticle inks such as silver, graphene oxide, cellulose nanofibers, carbon nanotubes [1, 2, 52, 53] and is not restricted to QD inks. We note that the current work requires fluorescent inks for imaging, hence QDs have been chosen owing to their broad range of applications in the field of printed optoelectronics, such as LEDs [4]. The knowledge of soft matter physics gained from this study can then be leveraged to understand how the change in shape and size of nanoparticles affects the change in printed features, potentially extending the result to include non-fluorescent nanoparticles in future works. Standard morphology characterisation techniques such as scanning electron microscopy require extensive sample preparation such as Au–Pd coating to reduce charging, and cross-sectional dicing of the sample. In another example, atomic force microscopy requires an extensive sampling time to raster

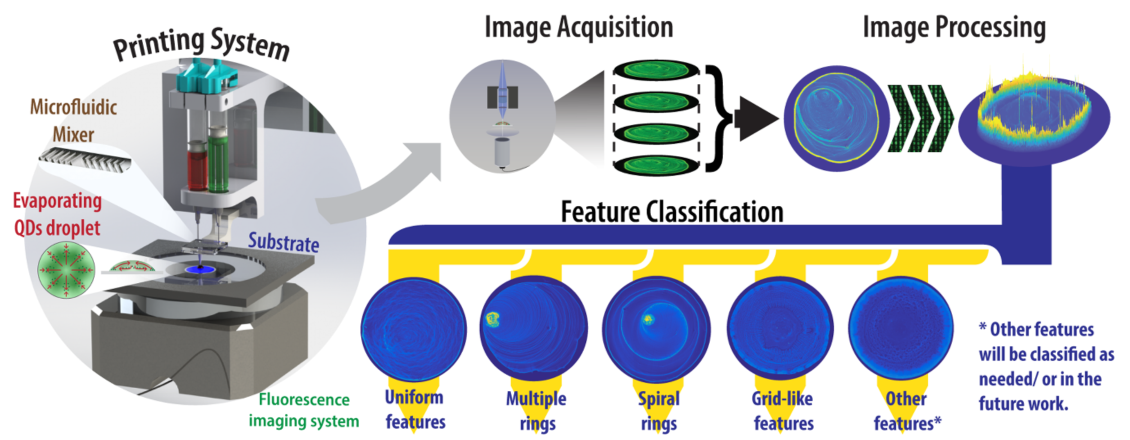

Figure 1. Schematic illustrations of a microfluidic mixer-based printing and fluorescence imaging platform capable of printing colloidal inks of varying concentration and solvent to co-solvent ratio. The imaging platform captures the samples under fluorescence microscope and performs feature classification into five class labels to identify samples based on internal textures.

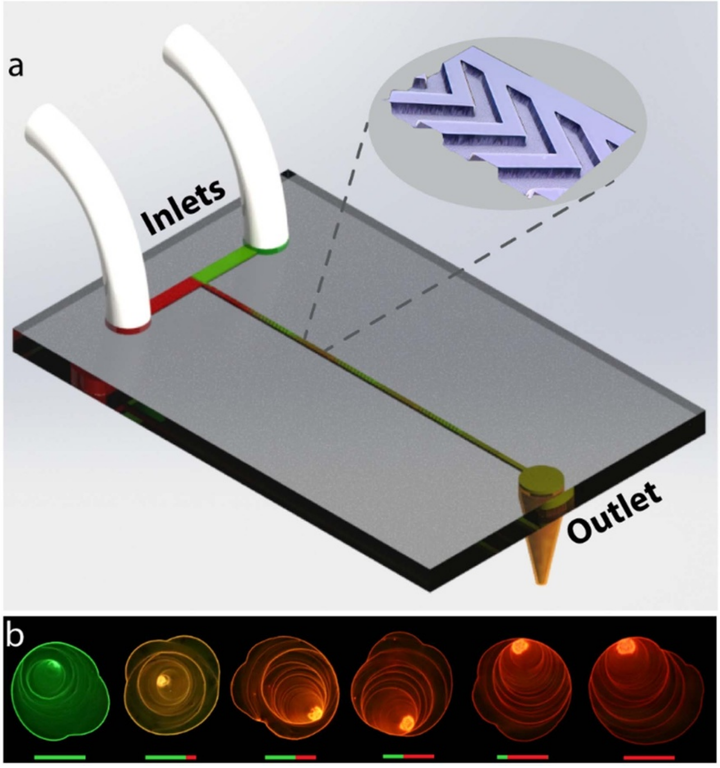

Figure 2. Herringbone microfluidic mixer (a) 3D model of the mixer, where the inset shows the profilometry measurement of the microfabricated Herringbone microstructure (height of 120 μm and width of 100 μm). (b) Fluorescence images of the printed QDs from the mixer with red (620 nm) and green (540 nm) QD inks at 1 mg ml^{-1} concentration with mixing ratios ranging from 0% to 100% at 20% intervals. The colour bars below the samples indicate the volume percentage of the type of QDs present in each sample.

the entire millimetre-scale sample (>10 hr). On the other hand, our printing and imaging platform allows a rapid (∼14 min), non-invasive *in situ* characterisation on the printed droplet; which provide the characterisation of distinct pattern resulting from the change of composition prior to further characterisation of selected representative samples.

As a proof of concept, we demonstrated the capabilities of the mixer-based print platform using ink composition (concentration and solvent–cosolvent ratio (SCR)) as the dominant print parameters. As shown by the representative sample space in figure 3, the system is capable of generating a broad range of microstructural features such as the so-called ‘coffee ring’ and grid-like features by modulating the ink composition. After processing the sample images captured from the fluorescent microscope, we classify each sample based on the internal textures by utilising a support vector machine (SVM) guided classification model. Further investigation and analysis

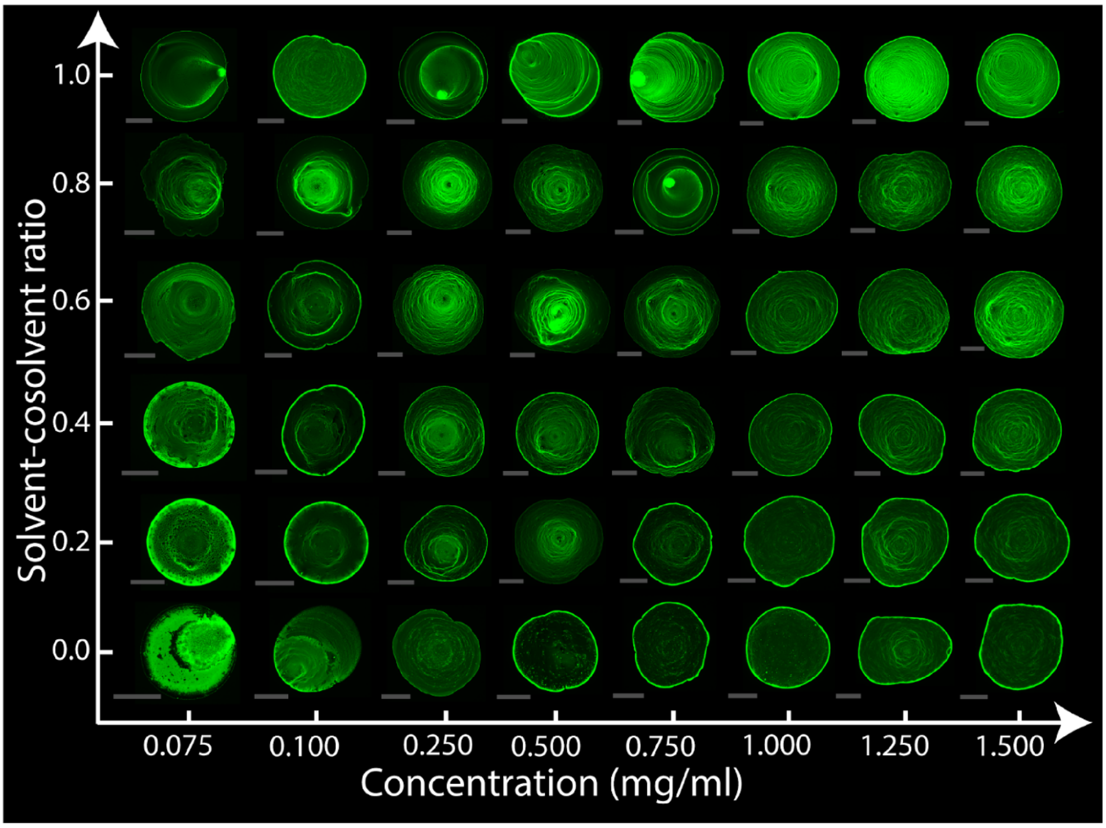

Figure 3. Representative data of printed QDs (540 nm) with toluene as solvent and dichlorobenzene as cosolvent from pure toluene (SCR = 1.0) to pure dichlorobenzene (SCR = 0.0), in concentrations ranging from 0.075 mg ml^{-1} to 1.500 mg ml^{-1}. For this representation, the exposure of the samples has been adjusted to visualize the variance of the printed features. The scale bars are 705 μm.

of the relationship between the drop textures and print parameters can provide insight to elucidate the underlying mechanisms of nanoparticle assembly. We envision the outcome of this study can enable an autonomous machine-learning driven print platform that adapts to microenvironmental perturbations.

2. Materials and methods

2.1. Micromixer fabrication and interfacing

Two-step photolithography was performed on a silicon wafer to fabricate the herringbone patterns of the chaotic mixer [54], as shown in figure 2(a). We used laser micromachining (Universal Laser Systems, Scottsdale, AZ, USA) to drill access holes in a Pyrex wafer for interfacing inlet and outlet tubes (800 μm ID, Cole Parmer, IL, USA) with the micromixer. The cleaned Pyrex wafer was anodically bonded with the silicon wafer containing the mixing structures. A diamond dicing blade was used to dice the individual mixers before interfacing with Teflon tubes using heat and adhesives as described in [55].

2.2. QD preparation

Stock solutions of 10 mg ml^{-1} of QDs (CdSe/ZnS core/shell QD solid, Ocean Nano Tech, CA, USA) are prepared with toluene and dichlorobenzene and sonicated for 30 min. Ink concentrations ranging between 0.075–0.1 mg ml^{-1} at 0.025 mg ml^{-1} intervals and between 0.25–1.5 mg ml^{-1} at 0.25 mg ml^{-1} intervals are then generated using the integrated microfluidic mixer. A micro-syringe pump is used to fine-tune the flow volume of the QD stock solution with its corresponding solvent (toluene or dichlorobenzene). In addition to concentration changes, the SCRs of toluene and dichlorobenzene is varied between 0.0 and 1.0 at intervals of 0.2, where 0.0 corresponds to 100% dichlorobenzene and 1.0 corresponds to 100% toluene.

2.3. QD printing

The flow rate and flow duration of the micro-syringe pumps are adjusted to generate the above-mentioned compositions by precise mixing of QD inks.

A custom Python code is adapted [54] to control both the pumps and the three-axis micro-positioning gantry (Aerotech, PA, USA). RS-232-to-USB connectors are used to interface the microsyringe pumps with the PC and the gantry system is interfaced using a PCIe FireWire adapter. Serial communication protocol is used to control the hardware from the PC. The Python code controls the flow duration and flow rate while the print is in motion, providing comprehensive control of the printing parameters. Assisted by the three-axis micro-positioning gantry with a custom G-code, QD droplets are printed using a 25-gauge needle (GA) at a constant height of 80 μm from the substrate. For substrate, we used glass slides cleaned using acetone and isopropyl alcohol and dried using compressed nitrogen gas. The printed droplets are evaporated at ambient temperature and humidity (21 °C ± 1 °C and 30 ± 2 RH%) prior to the imaging.

2.4. Sample imaging

The evaporated samples are imaged under an inverted fluorescence microscope (DMI8, LEICA Microsystems, Germany). The data is plotted with green colour using Las X software (Leica Microsystems, Germany) to aid sample visualisation. We note that the intensity information obtained from each pixel is preserved regardless of the choice of colour for visualisation.

The samples are imaged with an exposure time ranging from 10 to 300 ms at 10 ms intervals, 300 to 950 ms at 50 ms intervals, 1000 to 3000 ms at 100 ms intervals, and 3000 to 5000 ms at 1000 ms intervals which are automated by a custom Python code. The samples are imaged in multiple exposures to increase the dynamic range, which can provide additional spatial deposition information. For example, an 'overexposed' image can reveal delicate features not identified at lower exposure, while an 'underexposed' image can preserve information from thicker features with higher photoluminescence intensity.

The captured fluorescent images of each sample were then qualitatively labelled as one of five classes based on their relative difference of internal texture observed in our training data set, as shown in figure 4. For the training data set, the observed dominant features were selected as the basis of our class labels, most of which have been described in earlier literature. We observed features that exhibit relatively lower variation of internal deposition texture without the presence of internal 'coffee ring' like deposition and classified them as '*uniform*'. Features exhibiting multiple coffee ring depositions are classified as '*multiple coffee rings*'. Ring-like depositions are also observed that are distinct from multiple rings and form a spiral deposition pattern, which we classified as '*spiral coffee rings*'. Similarly, samples exhibiting radial and ring deposition formed grid-like patterns and are labelled as '*grid-like*'. Samples that exhibited features distinct from the above-mentioned classes are not included in the scope of the current work and are labelled as '*others*'.

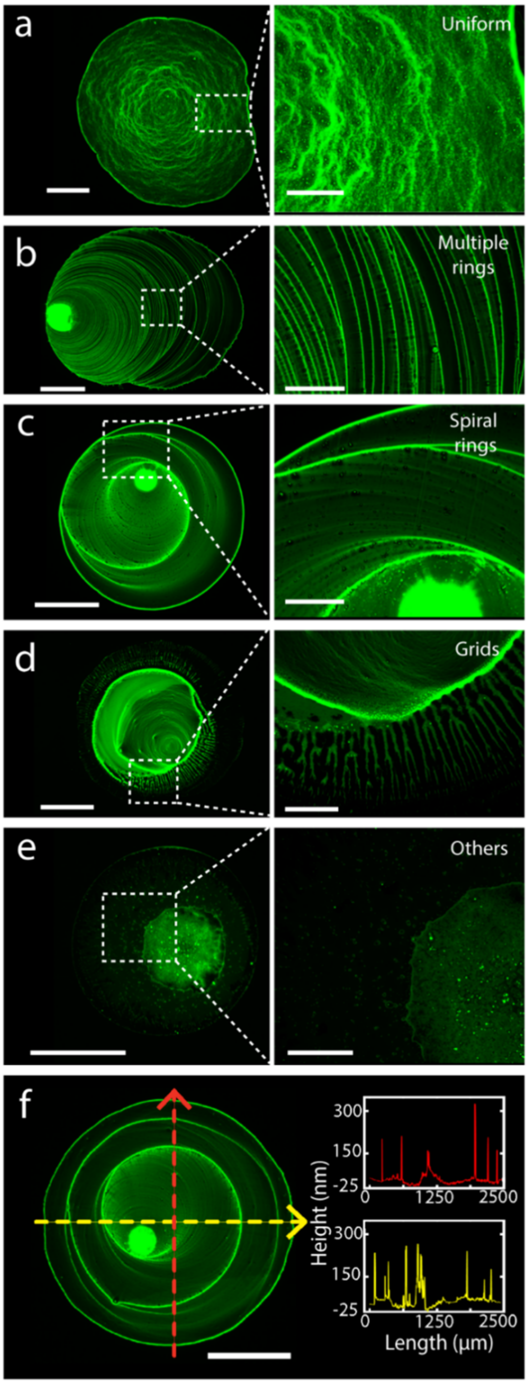

Figure 4. Fluorescence microscopy images showing the internal features of evaporative-driven 3D printed QDs: (a) a fully coated, relatively 'uniform' internal texture, (b) multiple 'coffee rings', (c) spiral ring patterns, (d) grid-like patterns, and (e) other features. The right-hand column shows the closeup of the pattern to its immediate left. The scale bars on the left are 705 μm. The scale bars on the right column are 176 μm. (f) Analysis of the physical deposition thickness of the sample. The graphs show profilometry measurements of the sample across the yellow (horizontal) and red (vertical) lines. The scale bar is 705 μm.

2.5. Image processing and feature engineering

The experimental protocols described earlier produce an extensive dataset. For each printed drop, these protocols produce a dataset containing 86 images taken at different times in the printing process, with each image being 1296 × 966 pixels. Various image processing and feature engineering approaches have been explored in this study to evaluate their efficacy in capturing the salient details of the texture (i.e. spatial deposition patterns) in the printed drop. Building on earlier work in the feature engineering of the material internal structure [56, 57], we have leveraged

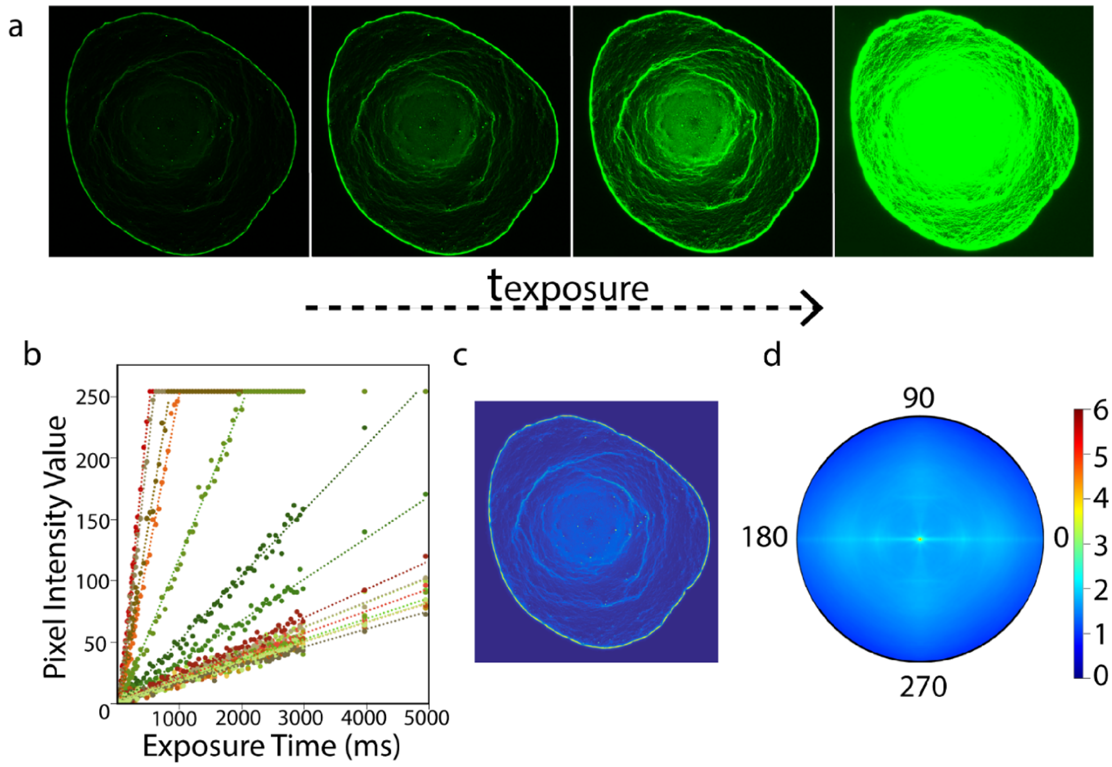

Figure 5. Data pipeline schematic showing (a) an array of images with increasing exposure times used to create, (b) the intensity map and determine (c) spatial deposition density plot. (d) Spatial correlations used to create feature map, a standardized representation allowing for comparison of important information to drying pattern recognition. The intensity map at (b) is a representative plot of twenty randomly selected pixels from a sample.

the framework of spatial correlations to quantify the spatial patterns in the printed drop.

The 1st step in the feature engineering of the printed drop images is to establish appropriate measures of interest at the scale of individual pixels.

Figure 5(a) shows an example set of images, where each image shows the characteristic textures discussed earlier. Figure 5(b) shows the variation of intensity at selected pixels through exposure time in this set of images. It became clear from such plots that the intensity at each pixel increases approximately linearly until the maximum intensity is obtained. The maximum intensity in the images is limited to a value of 255. This is reflected as saturation (i.e. intensity plateau) in figure 5(b). This saturation is due to the physical limitation of the camera sensor pixels reaching their charge storage capacity [56]. Based on the linear response before saturation in figure 5(b), it was decided to adopt the average intensity rate (i.e. the average slope of the intensity versus exposure time before the maximum intensity is reached) as the primary pixel-scale measure of interest for our study. Physically, this measure corresponds to the pixel-scale deposition density of the photoluminescent material. An example of a pixelised map of the deposition density is shown in figure 5(c). This plot shows a characteristic texture that could be used to classify automatically using AI tools, the diverse printed drops imaged in our experiments.

The deposition density plots of the type shown in figure 5(c) are still high dimensional in that they require an array of 1296 × 966 real numbers. In the present work, our interest is restricted to identifying features that could be easily computed and utilised to classify the images primarily based on the details of the observed deposition spatial patterns (i.e. textures) in the printed drops. We have designed and implemented a computational protocol comprising the following steps to address this challenge: (a) drop boundary identification, (b) deposition density calculation, (c) size and intensity normalisation, (d) computation of spatial correlations, and (e) dimensionality reduction.

The 1st step, drop boundary identification, removes any detached ink spots and identifies the specific set of pixels where all of the next steps in the feature engineering analyses will be performed. The drop boundary identification is accomplished in this study using a canny edge detection algorithm [58], which identifies pixel-to-pixel intensity gradients above a certain threshold. The highest exposure time (5000 ms) image is utilised for this step due to the high contrast between the printed drop and the dark background. Discontinuities in the detected edges were filled with a morphological closing operation [59], which involves a process of expansion followed by shrinkage of the features of interest (in this case, the drop boundary). This operation allows for nearby but unconnected pixels of the drop boundary to join during the expansion step and remain connected as the subsequent shrinking step removes the other excess pixels. With the fully connected boundary, a morphological region filling operation [59] is performed to fill the interior of the drop boundary, thus identifying all pixels belonging to the printed drop. Any satellite ink drops identified outside the primary drop are removed. The aforementioned edge detection and morphological processing operations were in Python using a combination of OpenCV [60], Scikit-image [61] and SciPy [62] packages.

Next, the deposition density is computed for only the pixels in the primary printed drop. The pre-saturation intensities at each pixel are fit to a linear expression in time with a zero intercept to estimate its deposition rate. A deposition density of zero is assigned to all background pixels. Deposition density plots of the kind shown in figure 5(c) were created for each printed drop.

Normalisations were performed on each deposition density map to ensure that the information relevant to the texture classification problem is prioritised in our feature engineering effort. Our main strategy here is to de-emphasise or remove all other differences (other than texture in the printed drops) between the deposition density maps from the different drops. Specifically, we devised computations for normalising the deposition rate maps, in which all printed drops were adjusted to exhibit the same size and the same average intensity. As a result of this normalisation, the differences in spatial ink patterns become the main differentiators between the normalised deposition rate maps. The size of the printed drops was standardised by scaling each printed drop to a size of 700 000 pixels. This was done by scaling each deposition rate image by the square root of the ratio of 700 000 to its number of printed drop pixels. The 700 000-pixel target drop size was selected to maximise the size of the drop in the image without cropping any samples. Intensity normalisation was then accomplished by dividing each deposition density map by its average intensity. The result of these adjustments is a standardised deposition density map with an average intensity of one and a size of 700 000 pixels.

The texture in the standardised deposition density maps is quantified in this work using the framework of spatial correlations [57], which has been used extensively in prior work on the quantification of spatial heterogeneity in material microstructures [63–66]. A specific variant of spatial correlations called rotationally invariant spatial correlations [67] is used here. They effectively filter out any arbitrary in-plane rotation of the image while preserving the anisotropy of the morphological features and their relative placement in the image. As an example, the rotationally invariant autocorrelation map for the deposition density map in figure 5(c) is shown in figure 5(d). These feature maps contain autocorrelation information in polar coordinates with the dominant information-oriented at 0°. It is this reorienting that produces the desired rotational invariance. Full details of this approach can be found in Cecen *et al* [67].

Example feature maps for printed drops of the five classes identified earlier are shown in figures 6(a)–(f). These information-dense feature maps capture a multitude of salient measures of the spatial deposition patterns. The most significant information in the feature maps lies in the central peak, whose intensity and width capture salient information on the spatial uniformity of the deposition rate in the printed drop. An increase in the intensity of the central peak corresponds to less uniform deposition. This is most clearly seen by comparing sample (b) with the other samples. Sample (b) indeed exhibits the highest central peak intensity and the most non-uniform deposition pattern. On the other hand, sample (e) exhibits the lowest central peak and the most uniform deposition pattern. Although samples (a) and (f) also display high central peak intensities (suggesting relatively higher levels of non-uniform deposition patterns), their peaks are significantly narrower than for sample (b). In auto-correlations, the width of the central peak roughly corresponds to the feature size in the pattern. Indeed, there is a large feature in sample (b) (the yellow agglomeration in the deposition pattern) that is responsible for the relatively wide central peak in its feature map. Similarly, the width of the central peak in the feature maps of samples (a) and (f) corresponds well with the thickness of the thin perimeter rings.

The next important subset of features in the feature map is in the prominent radial line, which extends horizontally outwards from the central peak at 0° and 180°. This horizontal line contains directionally averaged auto-correlation information about the deposition pattern. Thus, as samples become increasingly uniform, this horizontal line displays radial decay and becomes the main characteristic in the feature map. This is most clearly observed in the feature map of sample figure 6(a), which exhibits a mostly uniform deposition pattern, except for the thin outer ring. Alternatively, samples with non-uniform deposition patterns, such as samples (b) and (f), do not display smooth radial decay profiles. Morphological anisotropy in the deposition patterns is captured in the rest of the feature map (i.e. in the top and bottom halves of the feature maps). Samples (c) and (d) display the most anisotropy in their deposition pattern. Similarly, sample (b) displays high anisotropy because of the eccentric ring deposition pattern. Conversely, samples (a), (e) and (f) display relatively little morphological anisotropy in their deposition patterns. For successful classification, samples of the same class should display similar feature map attributes. Spiral coffee

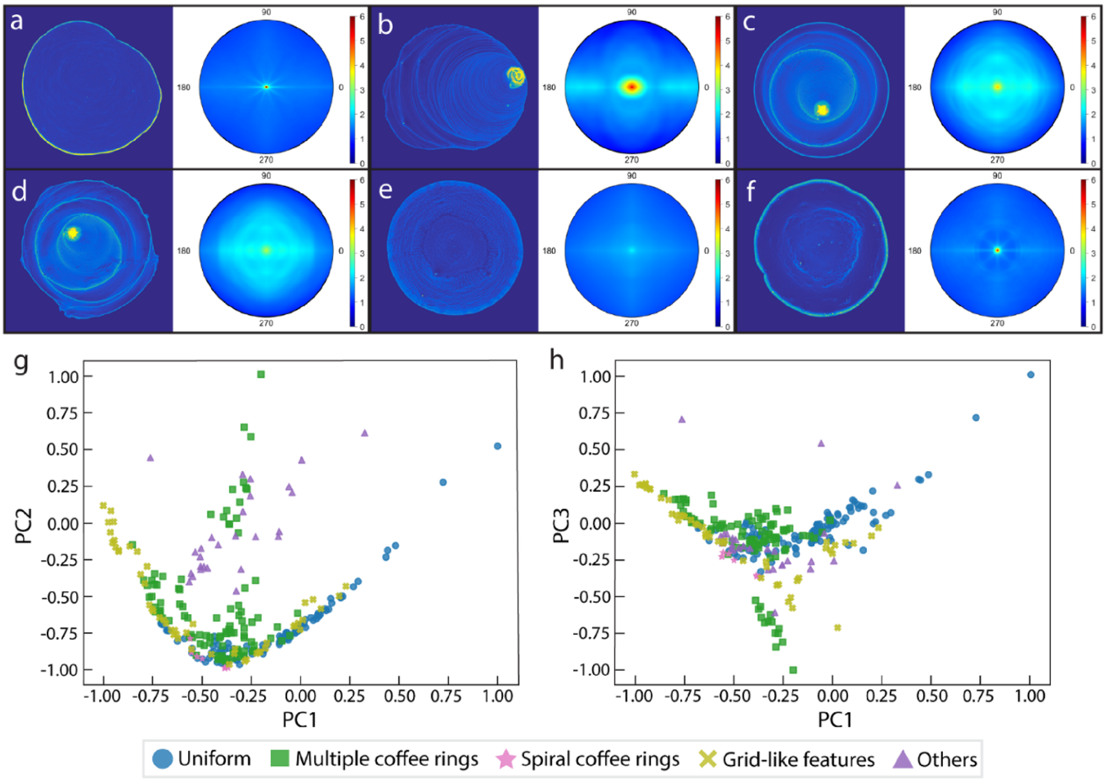

Figure 6. Example deposition density plots and corresponding rotationally invariant feature maps for the different classes of printed drops studied in this work: (a) uniform, (b) multiple coffee rings, (c–d) spiral coffee rings, (e) grid-like features, and (f) others. (g–h) Selected principal component (PC) projections of the rotationally invariant autocorrelations of the normalized deposition rate maps for all samples included in this study.

ring samples (c) and (d) show that this expectation is met as despite differences in drop shape and nuances of the spiral coffee ring structures, the feature maps display similar central peaks, horizontal profiles and anisotropic information.

The feature maps shown in figures 6(a)–(f), while providing the desired translation and rotation invariances, still require an 875 × 656 array of features. While half of the features in an auto-correlation map are redundant due to their centro-symmetry, the number of independent features is still unwieldy for classifying the large ensemble of images aggregated in this study. Following prior work on microstructure classification [63, 68, 69], PC analysis was performed on the entire collection of the feature maps to reduce their dimensionality. The low-dimensional projections of the PC space, shown in figures 6(g) and (h), reveal that some classes are beginning to separate in the 1st three dimensions. For example, figure 6(g) shows that PCs one and two separate the spiral coffee rings class from the majority of the other four classes. Similarly, figure 6(h) shows that PCs one and three separate certain subclasses of multiple coffee rings class. Indeed, a larger number of PCs than can be visualized would be needed to separate all of the different classes of the deposition patterns in our dataset.

2.6. Classification models

Both a SVM Classifier [70] and Random Forest (RF) Classifier [71] were used to classify the printed drop patterns based on their PC scores. The PC scores for each sample were provided as a one-dimensional vector. The optimal model hyperparameters and number of PCs were found by comparing through grid-search using five-fold cross-validation with ten repetitions considering both absolute prediction accuracy and balanced prediction accuracy as performance metrics. Due to the unbalanced nature of our dataset, resampling is necessary to balance the number of samples in each class and ensure that the fit of a classification model was not biased towards over prioritising predicting the majority classes. Resampling was conducted on the training sets through synthetic minority over-sampling technique (SMOTE) [72] which creates synthetic data points by interpolating between nearest neighbours within a class. Nine PCs was found to be optimal for both classification models. Since much of the minority class data is synthetic, it was ensured that the synthetic samples were only used in model training. Modelling and validation were done using the Scikit-learn package [73], and SMOTE resampling was done using the imbalanced-learn package [74]. Optimal RF parameters were found to be 250 estimators with a maximum depth of

12 and minimum of five samples per split. Optimal SVM performance was found using the RBF kernel with $C = 100$ and $\gamma = 1$. All image processing, feature engineering and modelling was completed on a desktop PC with an Intel Xenon E5-1607 CPU (3.00 GHz), 16 GB RAM and Nvidia Quadro K4000 graphics card.

3. Results and discussion

3.1. Micromixer

In contrast to 'manual mixing' of ink compositions that require preparation prior to printing, the microfluidic mixer can enable computer-controlled mixing *in situ* to enable a real-time ink composition modulation during the printing process. This enables the rapid exploration of a large number of ink compositions based on analysis of the printed patterns without human interaction.

As a proof of concept, we demonstrate that the microfluidic mixer allows us to rapidly explore 48 combinations of print parameters by switching ink compositions between (a) toluene and dichlorobenzene and (b) ink concentrations between 0.075 mg ml^{-1} and 1.500 mg ml^{-1}. The mixer platform is capable of mixing multiple nanoparticle inks of varying sizes of nanoparticles. The wavelength of emitted light from photoluminescent QD inks is dependent on the size of the nanoparticles. An increase in the nanoparticle size shows an increase in the wavelength of photoluminescence [75]. In figure 2(b), we observe the gradual transition of emitted colour from green to red which is a consequence of the mixing of the different sizes of nanoparticles by the micromixer. QSP 540 emits a wavelength of 540 nm, and QSP 620 emits a wavelength of 620 nm. We note that to capture the colour changes of the printed drop patterns, the images were captured using a DSLR camera (Canon EOS 80D) with a UV filter (Altura, FL, USA) under the illumination of UV light (∼410 nm).

3.2. Printed self-assembly patterns

The sample space with representative data of each ink composition is illustrated in figure 3. Figure 3 also highlights the entire parameter space and how the change in print parameters generate the five feature classes, as mentioned earlier.

When a droplet evaporates in ambient conditions, there is competition between different forces such as the contact line pinning due to the irregularities on the substrate, surface tension gradient between two different solvents, and de-wetting phenomenon [76, 77]. During evaporation, the solvent at the edges is replenished from the interiors of the droplet. A radially outward capillary flow induces the movement of the nanoparticles towards the edges [8]. This phenomenon produces the so-called 'coffee ring' feature at the drop edges, which can be reversed by introducing a strong Marangoni flow [78]. The ink composition can be varied by introducing a binary solution to induce a surface tension gradient and modulate the flow towards the centre [79, 80]. When the Marangoni flow becomes strong enough to redistribute the particles back to the centre, the nanoparticles are distributed rather uniformly compared to other patterns, leading to a relatively **uniform feature**, as shown in figure 4(a). As discussed earlier, we classified it as '*uniform*' as these features exhibit lower variation of internal textures observed in other sample classes such as *multiple rings* and *spiral rings*, as seen in figures 4(b) and (c). We do not imply that the feature has achieved the uniformity observed in the conventional manufacturing approaches, such as spin coating [81] or contact printing [82–84].

The **multiple ring patterns** indicate the deposition of multiple contact line deposits as the contact line recedes from the edge. As the nanoparticles are deposited at the receding contact line, the pinning force increases. This process leads to a stick-and-slip motion pinning the contact line long enough to form a substantial contact line deposit. Notably, the ring features are created when the contact line is stationary and not when the contact line is in motion [85]. This phenomenon has also been observed and discussed in earlier literature [41, 85–87]. In our printed sample space, the samples printed at concentrations of 0.500 mg ml^{-1} and 0.750 mg ml^{-1} for $\text{SCR} = 1.0$ exhibit clear *multiple* ring patterns. A detailed closeup view of the pattern is illustrated in figure 4(b).

The **spiral coffee ring** features are illustrated in figure 4(c), which shows the presence of ring-like deposits forming a spiral pattern, unlike well-defined rings, as in the case of *multiple coffee rings*. This is created when there is an imbalance of forces on the contact line, generating a spiral pattern instead of complete rings. Chen *et al* discussed that a counterbalance of surface tension and friction from the deposited particles with the substrate determines the contact line motion. When the contact line experiences an asymmetry of forces, such a spiral ring pattern is deposited [88]. This asymmetry of forces translates from the inhomogeneity of the surface and the friction of the drying nanoparticles with the substrate. As observed in figure 3, when we increase concentration without adding cosolvent ($\text{SCR} = 1.0$), we notice a transition from spiral coffee rings to a peripheral coffee ring with a relatively uniform internal texture. This is aligned with our understanding from earlier research as the increase in concentration increases pinning force and reduces the continuous depinning of the contact line.

Figure 4(d) shows the **grid-like feature**, which are a combination of radial lines and coffee rings forming a grid-like pattern. These features are usually created by a de-wetting mediated phenomenon at the drying front of the evaporating droplet. This can potentially be explained by earlier literature [85] as the grid-like

Table 1. Performance metrics and their standard deviations (SDs) for the classification models built in this work.

	Accuracy (%)	Accuracy SD (%)	Balanced accuracy (%)	Balanced accuracy SD (%)
Random forest	82.00	4.92	79.59	7.63
SVM	83.48	4.45	81.96	8.87

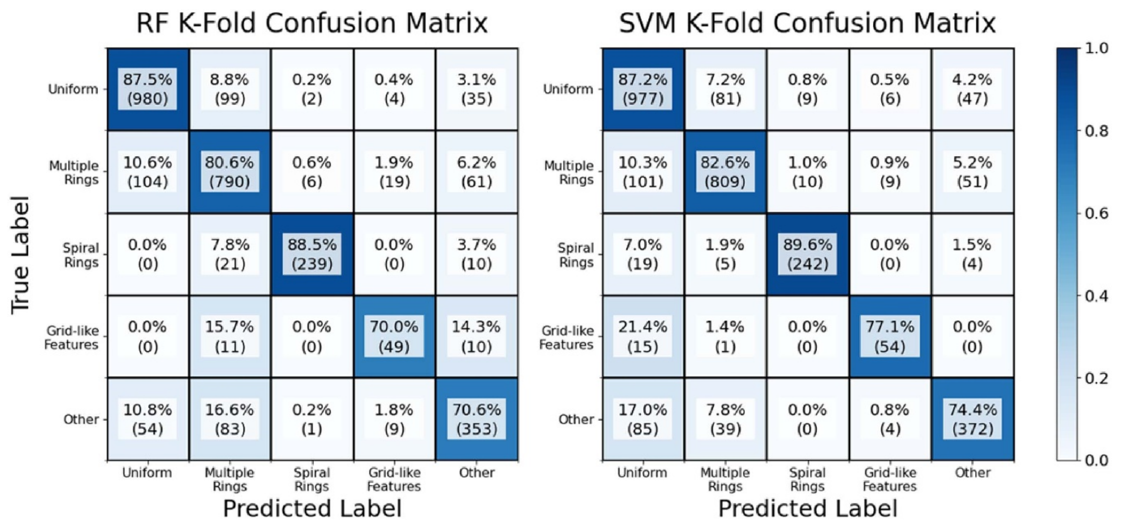

Figure 7. Confusion matrices for RF and SVM classification models.

features are formed by the steady de-wetting motion and the stick-slip motion of the contact line. When the contact line is stationary, it produces the ring-like deposition, and during the stick-slip motion, the radial lines are produced. This has been observed when cosolvent is mixed with the solvent (SCR is approximately 0.6–0.8), where competition between de-wetting effects, surface gradient and contact-line pinning forces have produced grid-like features at concentrations less than 0.750 mg ml^{-1}.

Apart from this, we also noticed the formation of patterns clearly distinguishable from the other observed features, as shown in figure 4(e), which we classified as '**other**' features. For example, the shape and texture of samples (at concentration = 0.075 mg ml^{-1} and SCR = 0.6 and 0.8) are distinct from the four studied classes in figures 4(a)–(d). Observed features such as the bull's-eye-like pattern (at concentration = 0.500 mg ml^{-1} and SCR = 0.2) and incomplete ring-like features (at concentration = 0.100 mg ml^{-1} and SCR = 0.6 in figure 3) have been described in earlier literature [85, 87]. However, features such as the ones observed at concentration = 0.075 mg ml^{-1}, SCR = 0.0 and 0.6 are, to the best of our knowledge, not discussed in earlier work [41, 85–89]. Future work on improving the classification model to identify previously unexplored features can provide valuable insight into understanding their governing physics.

Here we also note that the type of feature desired for 3D printing can vary based on target application. For example, a relatively uniform print feature is preferred for 3D printing of active layer in printed devices (such as LED), as demonstrated in previous research [4]. Other features such as the coffee ring and de-wetting effects have been explored in flexible printed transparent conductors [90–92] and optoelectronic devices [93, 94]. For example, coffee ring features have been leveraged to print high resolution transparent printed conductors [95]. Here, we focus on establishing a platform that can print and analyse a broad range of evaporation-driven patterns. The integrated feature analysis can provide valuable physical insights of the complex deposition behaviour, and ultimately can enable the ability to autonomously print a specific targeted feature in the future work.

3.3. Feature classification

We have demonstrated the results of both RF and SVM classification models for the feature classification approach. The RF and SVM classification models exhibit nearly identical performance, with the SVM displaying slightly higher accuracy (table 1). The accuracy values presented in this table summarise the overall performance of the models on the full dataset regardless of class. Balanced accuracy weights the accuracy of each class, irrespective of the number of data points in each class. Class-wise performance details of each model are presented in figure 7. The *uniform*, *multiple coffee rings* and *spiral coffee rings* classes were the most accurately classified archetypes for both models. The success in classifying *spiral coffee* *rings* is likely due to the relatively low intra-class variance observed in this class. Interestingly, the bulk of misclassifications for the *uniform* and *multiple coffee rings* samples were mistaken for each other. Much of these errors are likely due to the frequently observed transitional behaviour between well-defined *multiple coffee rings* and well-defined *uniform* texture. Transition behaviour occurs when defining elements of multiple classes are present within a single sample resulting in increased ambiguity. The *grid-like* features and *other* classes, on the other hand, proved to be the most difficult to classify. The difficulty in predicting *grid-like feature* is not surprising as this class had drastically fewer samples than the other classes and displayed notable variation within the class. This higher intra-class variance manifested in the form of transitional behaviour in which some samples displayed only low-contrast, localised grid behaviour mixed with features representative of the *other* class as opposed to other samples that displayed well-defined grid-like behaviour throughout. The *other* class samples errors were relatively evenly distributed between the *uniform* and *grid-like features* class. Errors in the other class are the most difficult to diagnose as this class tends to be a catchall for a variety of poorly understood behaviours.

The most significant challenge encountered during classification was the prevalence of samples that displayed characteristics of multiple classes. These multi-class samples were most commonly found in transitional regions of the parameter space. Upon further examination of the voting results of the RF classifier, it was found that amongst the samples that were misclassified, roughly 45% of such samples displayed a predicted probability of >30% for the true class. This observation validates the overall approach taken in this work. Improved feature engineering (e.g. deep-learning-based feature learning [96]) and multi-label classification approaches [97, 98] might be the next logical considerations for future work.

The data collection strategy for this work was based on a uniform exploration of the parameter space. While this sampling scheme does aid in developing a broad understanding of the drop characteristics as a function of the formulation parameters, it does not necessarily provide the best training data for a classification model. This is due to the possibility of under-sampling classes that appear in only tight parameter windows and over-sampling classes that appear across broad parameter ranges. Other sampling strategies based on active learning (e.g. uncertainty-based sampling [99] or expected model change [100]) are likely to improve the predictive accuracy of the classification models.

It should also be noted that the present effort was focused on classifying drops by the spatial characteristics of the internal ink deposition. However, numerous other characteristics of interest exist in the printed drops, including peripheral instabilities, agglomerations, and shrinkage. Shape moments and characterisation of the shrinkage from initial print size are likely to improve our system to identify the ‘other’ features better. Successfully identifying these characteristics would require these additional customisation of the feature engineering and classification approaches described above.

4. Conclusion

In conclusion, we have demonstrated the classification of printed textures using a novel printing and ML workflow. The workflow developed enables targeting desired textures via *in situ* ink composition tuning and classification. This model was generated based on 48 combinations of print parameters by switching ink concentrations and compositions between toluene and dichlorobenzene to generate evaporative-driven nanoparticle features. Such a broad range of formulations was made possible by our microfluidic mixer-based print platform, which can rapidly tune ink compositions and generate a diverse palette of deposition patterns. Finally, we classified the deposited patterns into five classes by studying the spatial characteristics of the internal textures. Our SVM model has achieved a balanced accuracy of 81.96% in classifying the internal textures of the evaporation-driven printed droplets.

The printing system and image classification protocol created in this work serve as the first steps towards the authors’ ultimate vision of building an automated process parameter control platform for evaporative patterning. Future work on the AI component will focus on developing a relationship between print parameters and printed drop textures. This knowledge will inform *in situ* control, allowing users to achieve targeted print patterning. Additional future improvements would involve considering the shape and size information of the printed droplets to improve the classification model’s accuracy. We can leverage the information provided by the ML model to build a closed-loop system that can autonomously guide us to print targeted patterns. We envision that the developed print platform integrated with AI thus has the potential to autonomously adapt to perturbations to print multi-scale multilayer active electronics in complex and dynamic environments.

Data availability statement

The data that support the findings of this study are available upon reasonable request from the authors.

Acknowledgments

The authors thank Samuel Hales for valuable discussions and help with manuscript preparation. Professor Yong Lin Kong acknowledges support from the National Institutes of Health (NIH) NIBIB Trailblazer Award (Grant No. 1-R21-EB029563-01); Utah NASA Space Grant Consortium Fellowship; Utah NASA Space Grant Consortium Faculty Research Seed Funding Awards; University of Utah Research Incentive Seed Grant Program; National Science Foundation (NSF) under Emerging Frontiers in Research and Innovation (EFRI) Program (Grant No. EFRI 1830958); 3M Non-Tenured Faculty Award; ORAU Ralph E. Powe Junior Faculty Award. Marshall Johnson acknowledges support from the Air Force Research Lab Minority Leader-Research Collaboration Program (UTC/AFRL) Contract FA8650-19-F-5830 and the National Science Foundation Graduate Research Fellowship Program Grant DGE-1650044. Professor Kalidindi acknowledges support from Vannevar Bush Fellowship with Office of Naval Research (ONR) Grant #N00014-18-1-2879. This work was performed in part at the Utah Nanofab sponsored by the College of Engineering, Office of the Vice President for Research, and the Utah Science Technology and Research (USTAR) initiative of the State of Utah. The author(s) appreciate the support of the staff and facilities that made this work possible.

ORCID iDs

Samannoy Ghosh https://orcid.org/0000-0002-8531-3043
Surya R Kalidindi https://orcid.org/0000-0001-6909-7507
Yong Lin Kong https://orcid.org/0000-0003-0270-2068

References

[1] Hales S, Tokita E, Neupane R, Ghosh U, Elder B, Wirthlin D and Kong Y L 2020 3D printed nanomaterial-based electronic, biomedical, and bioelectronic devices *Nanotechnology* **31** 172001

[2] Elder B, Neupane R, Tokita E, Ghosh U, Hales S and Kong Y L 2020 Nanomaterial patterning in 3D printing *Adv. Mater.* **32** 1907142

[3] Adams J J, Duoss E B, Malkowski T F, Motala M J, Ahn B Y, Nuzzo R G, Bernhard J T and Lewis J A 2011 Conformal printing of electrically small antennas on three-dimensional surfaces *Adv. Mater.* **23** 1335–40

[4] Kong Y L, Tamargo I A, Kim H, Johnson B N, Gupta M K, Koh T-W, Chin H-A, Steingart D A, Rand B P and McAlpine M C 2014 3D printed quantum dot light-emitting diodes *Nano Lett.* **14** 7017–23

[5] Meng X, Du J, Zhang H and Zhong X 2015 Optimizing the deposition of CdSe colloidal quantum dots on TiO_2 film electrode via capping ligand induced self-assembly approach *RSC Adv.* **5** 86023–30

[6] Bhowmik R, Berry R J, Durstock M F and Leever B J 2017 Prediction of the wetting behavior of active and hole-transport layers for printed flexible electronic devices using molecular dynamics simulations *ACS Appl. Mater. Interfaces* **9** 19269–77

[7] Sowade E, Blaudeck T and Baumann R R 2015 Inkjet printing of colloidal nanospheres: engineering the evaporation-driven self-assembly process to form defined layer morphologies *Nanoscale Res. Lett.* **10** 8

[8] Deegan R D, Bakajin O, Dupont T F, Huber G, Nagel S R and Witten T A 1997 Capillary flow as the cause of ring stains from dried liquid drops *Nature* **389** 827–9

[9] Meng L, Zeng T, Jin Y, Xu Q and Wang X 2019 Surface-modified substrates for quantum dot inks in printed electronics *ACS Omega* **4** 4161–8

[10] Zhang J, Zhu Z, Yu Z, Ling L, Wang C F and Chen S 2019 Large-scale colloidal films with robust structural colors *Mater. Horiz.* **6** 90–96

[11] Corker A, Ng H C H, Poole R J and García-Tuñón E 2019 3D printing with 2D colloids: designing rheology protocols to predict 'printability' of soft-materials *Soft Matter* **15** 1444–56

[12] Huang J, Segura L J, Wang T, Zhao G, Sun H and Zhou C 2020 Unsupervised learning for the droplet evolution prediction and process dynamics understanding in inkjet printing *Addit. Manuf.* **35** 101197

[13] Sun J, Bao B, He M, Zhou H and Song Y 2015 Recent advances in controlling the depositing morphologies of inkjet droplets *ACS Appl. Mater. Interfaces* **7** 28086–99

[14] Delli U and Chang S 2018 Automated process monitoring in 3D printing using supervised machine learning *Proc. Manuf.* **26** 865–70

[15] Mohamed O A, Masood S H and Bhowmik J L 2016 Optimization of fused deposition modeling process parameters for dimensional accuracy using I-optimality criterion *Meas. J. Int. Meas. Confed.* **81** 174–96

[16] Peng A, Xiao X and Yue R 2014 Process parameter optimization for fused deposition modeling using response surface methodology combined with fuzzy inference system *Int. J. Adv. Manuf. Technol.* **73** 87–100

[17] Nguyen T C, Can T T T and Choi W S 2019 Optimization of quantum dot thin films using electrohydrodynamic jet spraying for solution-processed quantum dot light-emitting diodes *Sci. Rep.* **9** 1–9

[18] Ball A K, Das R, Roy S S, Kisku D R and Murmu N C 2020 Modeling of EHD inkjet printing performance using soft computing-based approaches *Soft Comput.* **24** 571–89

[19] Guo Y, Peters J, Oomen T and Mishra S 2017 Distributed model predictive control for ink-jet 3D printing *2017 IEEE Int. Conf. Advanced Intelligent Mechatronics (AIM)* pp 436–41

[20] Sammons P M, Bristow D A and Landers R G 2015 A model predictive repetitive process control formulation for additive manufacturing processes

[21] Zomorodi H and Landers R G 2016 Extrusion based additive manufacturing using explicit model predictive control *2016 American Control Conf. (ACC)* pp 1747–52

[22] Stoyanov S and Bailey C 2017 Machine learning for additive manufacturing of electronics *Proc. Int. Spring Seminar on Electronics Technology* (IEEE Computer Society)

[23] Gu G X, Chen C and Buehler M J 2018 De novo composite design based on machine learning algorithm *Extreme Mech. Lett* **18** 19–28

[24] Chen C T and Gu G X 2020 Generative deep neural networks for inverse materials design using backpropagation and active learning *Adv. Sci.* **7** 1–10

[25] Gu G X, Chen C T, Richmond D J and Buehler M J 2018 Bioinspired hierarchical composite design using machine learning: simulation, additive manufacturing, and experiment *Mater. Horiz.* **5** 939–45

[26] Khanzadeh M, Chowdhury S, Marufuzzaman M, Tschopp M A and Bian L 2018 Porosity prediction: supervised-learning of thermal history for direct laser deposition *J. Manuf. Syst.* **47** 69–82

[27] Jin Z, Zhang Z and Gu G X 2019 Autonomous *in situ* correction of fused deposition modeling printers using computer vision and deep learning *Manuf. Lett.* **22** 11–15

[28] Jin Z, Zhang Z, Ott J and Gu G X 2021 Precise localization and semantic segmentation detection of printing conditions in fused filament fabrication technologies using machine learning *Addit. Manuf.* **37** 101696

[29] Wu M, Phoha V V, Moon Y B and Belman A K 2016 Detecting malicious defects in 3D printing process using machine learning and image classification *Emerging Technologies; Materials: Genetics to Structures; Safety Engineering and Risk Analysis* vol 14 (American Society of Mechanical Engineers)

[30] Zhang H, Moon S K and Ngo T H 2019 Hybrid machine learning method to determine the optimal operating process window in aerosol jet 3D printing *ACS Appl. Mater. Interfaces* **11** 17994–8003

[31] Jin Z, Zhang Z, Demir K and Gu G X 2020 Machine learning for advanced additive manufacturing *Matter* **3** 1541–56

[32] Wang C, Tan X P, Tor S B and Lim C S 2020 Machine learning in additive manufacturing: state-of-the-art and perspectives *Addit. Manuf.* **36** 101538

[33] Holzmond O and Li X 2017 *In situ* real time defect detection of 3D printed parts *Addit. Manuf.* **17** 135–42

[34] Hu H, He K, Zhong T and Hong Y 2019 Fault diagnosis of FDM process based on support vector machine (SVM) *Rapid Prototyp. J.* **26** 330–48

[35] Li Z, Zhang Z, Shi J and Wu D 2019 Prediction of surface roughness in extrusion-based additive manufacturing with machine learning *Robot. Comput. Integr. Manuf.* **57** 488–95

[36] Mireles J, Terrazas C, Gaytan S M, Roberson D A and Wicker R B 2015 Closed-loop automatic feedback control in electron beam melting *Int. J. Adv. Manuf. Technol.* **78** 1193–9

[37] Renken V, Albinger S, Goch G, Neef A and Emmelmann C 2017 Development of an adaptive, self-learning control concept for an additive manufacturing process *CIRP J. Manuf. Sci. Technol.* **19** 57–61

[38] Liu C, Chung A, Law C, Roberson D and Kong Z J 2019 Image analysis-based closed loop quality control for additive manufacturing with fused filament fabrication *J. Manuf. Syst.* **51** 75–86

[39] Isozaki A, Mikami H and Hiramatsu K *et al* 2019 A practical guide to intelligent image-activated cell sorting *Nat. Protocols* **14** 2370–415

[40] Anagnostidis V, Sherlock B, Metz J, Mair P, Hollfelder F and Gielen F 2020 Deep learning guided image-based droplet sorting for on-demand selection and analysis of single cells and 3D cell cultures *Lab Chip* **20** 889–900

[41] Gorr H M, Xiong Z and Barnard J A 2014 Pattern recognition for identification of lysozyme droplet solution chemistry *Colloids Surf.* B **115** 170–5

[42] Scime L and Beuth J 2018 Anomaly detection and classification in a laser powder bed additive manufacturing process using a trained computer vision algorithm *Addit. Manuf.* **19** 114–26

[43] Johnson M V, Garanger K, Hardin J O, Berrigan J D, Feron E and Kalidindi S R 2021 A generalizable artificial intelligence tool for identification and correction of self-supporting structures in additive manufacturing processes *Addit. Manuf.* **46** 102191

[44] Zhang Y, Soon H G, Ye D, Fuh J Y H and Zhu K 2020 Powder-bed fusion process monitoring by machine vision with hybrid convolutional neural networks *IEEE Trans. Ind. Inf.* **16** 5769–79

[45] Caggiano A, Zhang J, Alfieri V, Caiazzo F, Gao R and Teti R 2019 Machine learning-based image processing for on-line defect recognition in additive manufacturing *CIRP Ann* **68** 451–4

[46] Wang T, Kwok T-H, Zhou C and Vader S 2018 *In situ* droplet inspection and closed-loop control system using machine learning for liquid metal jet printing *J. Manuf. Syst.* **47** 83–92

[47] Ober T J, Foresti D and Lewis J A 2015 Active mixing of complex fluids at the microscale *Proc. Natl Acad. Sci.* **112** 12293–8

[48] Therriault D, White S R and Lewis J A 2003 Chaotic mixing in three-dimensional microvascular networks fabricated by direct-write assembly *Nat. Mater.* **2** 265–71

[49] Mansur E A, Ye M, Wang Y and Dai Y 2008 A state-of-the-art review of mixing in microfluidic mixers *Chin. J. Chem. Eng.* **16** 503–16

[50] Lee C Y, Chang C L, Wang Y N and Fu L M 2011 Microfluidic mixing: a review *Int. J. Mol. Sci.* **12** 3263–87

[51] Hardin J O, Ober T J, Valentine A D and Lewis J A 2015 Microfluidic printheads for multimaterial 3D printing of viscoelastic inks *Adv. Mater.* **27** 3279–84

[52] Zeng M and Zhang Y 2019 Colloidal nanoparticle inks for printing functional devices: emerging trends and future prospects *J. Mater. Chem.* A **7** 23301–36

[53] Ee L Y and Yau L S F 2021 Recent advances in 3D printing of nanocellulose: structure, preparation, and application prospects *Nanoscale Adv.* **3** 1167–208

[54] Stroock A D, Dertinger S K W, Ajdari A, Mezić I, Stone H A and Whitesides G M 2002 Chaotic mixer for microchannels *Science* **295** 647–51

[55] Pattekar A V and Kothare M V 2003 Novel microfluidic interconnectors for high temperature and pressure applications *J. Micromech. Microeng.* **13** 337–45

[56] Hasinoff S 2014 Saturation (imaging) pp 699–701

[57] Kalidindi S R 2015 Statistical quantification of material structure *Hierarchical Materials Informatics* (Oxford: Butterworth-Heinemann)

[58] Canny J 1986 A computational approach to edge detection *IEEE Trans. Pattern Anal. Mach. Intell.* **PAMI-8** 679–98

[59] Goyal M 2011 Morphological image processing *Int. J. Comput. Sci. Technol.* **2** 161–5

[60] Bradski G 2000 The OpenCV library *Dr Dobb's J. Softw. Tools* 122–5

[61] van der Walt S *et al* 2014 Scikit-image: image processing in Python ed S Gomez *PeerJ* **2** e453

[62] Travis E O 2007 Python for scientific computing *Comput. Sci. Eng.* **9** 10–20

[63] Choudhury A, Yabansu Y C, Kalidindi S R and Dennstedt A 2016 Quantification and classification of microstructures in ternary eutectic alloys using 2-point spatial correlations and principal component analyses *Acta Mater.* **110** 131–41

[64] Khosravani A, Cecen A and Kalidindi S R 2017 Development of high throughput assays for establishing process-structure-property linkages in multiphase polycrystalline metals: application to dual-phase steels *Acta Mater.* **123** 55–69

[65] Paulson N H, Priddy M W, McDowell D L and Kalidindi S R 2018 Data-driven reduced-order models for rank-ordering the high cycle fatigue performance of polycrystalline microstructures *Mater. Des.* **154** 170–83

[66] Iskakov A, Yabansu Y C, Rajagopalan S, Kapustina A and Kalidindi S R 2018 Application of spherical indentation and the materials knowledge system framework to establishing microstructure-yield strength linkages from carbon steel scoops excised from high-temperature exposed components *Acta Mater.* **144** 758–67

[67] Cecen A, Yabansu Y C and Kalidindi S R 2018 A new framework for rotationally invariant two-point spatial correlations in microstructure datasets *Acta Mater.* **158** 53–64

[68] Niezgoda S R, Kanjarla A K and Kalidindi S R 2013 Novel microstructure quantification framework for databasing, visualization, and analysis of microstructure data *Integr. Mater. Manuf. Innov.* **2** 54–80

[69] Sundararaghavan V and Zabaras N 2005 Classification and reconstruction of three-dimensional microstructures using support vector machines *Comput. Mater. Sci.* **32** 223–39

[70] Cortes C and Vapnik V 1995 Support-vector networks *Mach. Learn.* **20** 273–97

[71] Breiman L 2001 Random forests *Mach. Learn.* **45** 5–32

[72] Chawla N V, Bowyer K W, Hall L O and Kegelmeyer W P 2002 SMOTE: synthetic minority over-sampling technique *J. Artif. Intell. Res.* **16** 321–57

[73] Pedregosa F, Varoquaux G, Gramfort A, Michel V and Thirion B 2011 Scikit-learn: machine learning in Python *J. Mach. Learn. Res.* **12** 2825–30

[74] Kovács G 2019 Smote-variants: a Python implementation of 85 minority oversampling techniques *Neurocomputing* **366** 352–4

[75] Dabbousi B O, Rodriguez-Viejo J, Mikulec F V, Heine J R, Mattoussi H, Ober R, Jensen K F and Bawendi M G 1997 (CdSe)ZnS core-shell quantum dots: synthesis and characterization of a size series of highly luminescent nanocrystallites *J. Phys. Chem.* B **101** 9463–75

[76] Armstrong S, McHale G, Ledesma-Aguilar R and Wells G G 2019 Pinning-free evaporation of sessile droplets of water from solid surfaces *Langmuir* **35** 2989–96

[77] Li W, Lan D and Wang Y 2017 Dewetting-mediated pattern formation inside the coffee ring *Phys. Rev.* E **95** 042607

[78] Hu H and Larson R G 2006 Marangoni effect reverses coffee-ring depositions *J. Phys. Chem.* B **110** 7090–4

[79] Seo C, Jang D, Chae J and Shin S 2017 Altering the coffee-ring effect by adding a surfactant-like viscous polymer solution *Sci. Rep.* **7** 500

[80] Majumder M *et al* 2012 Overcoming the 'coffee-stain' effect by compositional Marangoni-flow-assisted drop-drying *J. Phys. Chem.* B **116** 6536–42

[81] Yang Y, Zheng Y, Cao W, Titov A, Hyvonen J, Manders J R, Xue J, Holloway P H and Qian L 2015 High-efficiency light-emitting devices based on quantum dots with tailored nanostructures *Nat. Photon.* **9** 259–65

[82] Ji T, Jin S, Zhang H, Chen S and Sun X W 2018 Full color quantum dot light-emitting diodes patterned by photolithography technology *J. Soc. Inf. Disp.* **26** 121–7

[83] Liu S, Liu W, Ji W, Yu J, Zhang W, Zhang L and Xie W 2016 Top-emitting quantum dots light-emitting devices employing microcontact printing with electricfield-independent emission *Sci. Rep.* **6** 1–9

[84] Lee B H and Sung M M 2007 Selective atomic layer deposition of metal oxide thin films on patterned self-assembled monolayers formed by microcontact printing *J. Nanosci. Nanotechnol.* **7** 3758–64

[85] Deegan R D 2000 Pattern formation in drying drops *Phys. Rev.* E **61** 475–85

[86] Kaya D, Belyi V A and Muthukumar M 2010 Pattern formation in drying droplets of polyelectrolyte and salt *J. Chem. Phys.* **133** 1–9

[87] Bhardwaj R, Fang X and Attinger D 2009 Pattern formation during the evaporation of a colloidal nanoliter drop: a numerical and experimental study *New J. Phys.* **11** 33

[88] Chen Y J, Suzuki K and Yoshikawa K 2015 Self-organized target and spiral patterns through the 'coffee ring' effect *J. Chem. Phys.* **143** 084702

[89] Ryu S A, Kim J Y, Kim S Y and Weon B M 2017 Drying-mediated patterns in colloid-polymer suspensions *Sci. Rep.* **7** 1–7

[90] Chopra K L, Major S and Pandya D K 1983 Transparent conductors—a status review *Thin Solid Films* **102** 1–46

[91] Hecht D S, Hu L and Irvin G 2011 Emerging transparent electrodes based on thin films of carbon nanotubes, graphene, and metallic nanostructures *Adv. Mater.* **23** 1482–513

[92] Kong Y L, Gupta M K, Johnson B N and McAlpine M C 2016 3D printed bionic nanodevices *Nano Today* **11** 330–50

[93] Bonaccorso F, Sun Z, Hasan T and Ferrari A C 2010 Graphene photonics and optoelectronics *Nat. Photon.* **4** 611–22

[94] Eda G, Fanchini G and Chhowalla M 2008 Large-area ultrathin films of reduced graphene oxide as a transparent and flexible electronic material *Nat. Nanotechnol.* **3** 270–4

[95] Shimoni A, Azoubel S and Magdassi S 2014 Inkjet printing of flexible high-performance carbon nanotube transparent conductive films by 'coffee ring effect' *Nanoscale* **6** 11084–9

[96] Jing L and Tian Y 2021 Self-supervised visual feature learning with deep neural networks: a survey *IEEE Trans. Pattern Anal. Mach. Intell.* **43** 4037–58

[97] Zhang M L and Zhou Z H 2014 A review on multi-label learning algorithms *IEEE Trans. Knowl. Data Eng.* **26** 1819–37

[98] Wei Y, Xia W, Lin M, Huang J, Ni B, Dong J, Zhao Y and Yan S 2016 HCP: a flexible CNN framework for multi-label image classification *IEEE Trans. Pattern Anal. Mach. Intell.* **38** 1901–7

[99] Sharma M and Bilgic M 2017 Evidence-based uncertainty sampling for active learning *Data Min. Knowl. Discov.* **31** 164–202

[100] Cai W, Zhang Y and Zhou J 2013 Maximizing expected model change for active learning in regression *Proc. IEEE Int. Conf. Data Mining, ICDM* pp 51–60